International Journal of Adhesion & Adhesives 102 (2020) 102675

Contents lists available at ScienceDirect

International Journal of Adhesion and Adhesives

journal homepage: http://www.elsevier.com/locate/ijadhadh

Advanced ultrasonic NDT for weak bond detection in composite-adhesive bonded structures

Bengisu Yılmaz [a,*], Elena Jasiūnienė [a,b]

[a] Prof. K. Baršauskas Ultrasound Research Institute, Kaunas University of Technology, K. Baršausko St. 59, LT, 51423, Kaunas, Lithuania
[b] Department of Electronics Engineering, Kaunas University of Technology, Studentu St. 48, LT, 51367, Kaunas, Lithuania

ARTICLE INFO

Keywords:
Composites
Non-destructive testing
Acoustic microscopy
Adhesive joints

ABSTRACT

Weak bond detection in composite-adhesive joints is a highly challenging task in the non-destructive testing (NDT) community. This paper aims to evaluate the bonding quality in composite-adhesive bonded structures with high-frequency high-resolution acoustic microscopy. Carbon fibre reinforced epoxy-epoxy bonded single-lap joints containing three different bonding quality -debonding, weak bond with less and more contamination, in addition to perfect bond were investigated. Shape-based feature extraction algorithm in the frequency domain was developed in order to detect weak bonds. The results show that high frequency focused transducers used in acoustic microscopy is a great choice to visualize interface quality in bonded structures. Developed post-processing algorithm performs well on the detection of weak bond, independent from the perfect bond inspection results.

1. Introduction

In emerging technologies such as aerospace, automotive, and marine, the usage for high strength-low weight engineering materials like composite materials has increased drastically as reported by Scarselli et al. [1]. Efficient bonding technologies for these materials is challenging because of their natural inhomogeneous design. As stated in the comprehensive review by Budhe et al. [2], adhesively bonded structures not only create high strength to weight ratio, but also allow homogenous load distribution, protect the structure against galvanic corrosion, preserve the structural integrity of composites, and keep the structure surface smooth. Moreover, adhesive joints allow to design complex shape bonded structures and join dissimilar materials. As Jasiuniene et al. [3] stated adhesive bonds in-between composite substrates has become more popular due to the potential fibre breakage, local damages, and residual stress occurring around rivets. Tornow et al. [4] agrees with the early work of Adams and Drinkwater [5] and declares the adhesive bonding as the optimum method to bond composite structures, however, its usage is limited due to inadequate evaluation of bonding quality by non-destructive testing methods.

Vine et al. [6] showed that non-destructive evaluation of adhesive joints is a complex task since the bonding is an interfacial phenomena that involves a very thin layer of material, mostly significantly lower than the ultrasonic wavelength that is used for inspection. Bonding quality depends on various factors in production phase such as surface preparation, wettability, environmental conditions (temperature – pressure – humidity), and the curing process. In addition, other defects may initiate or the previous defects might propagate in bonded structure as a result of fatigue and usage. Adams and Cawley [7] discusses the defect types and causations that can lead to structural failures in bonded structures such as delamination, porosity, moisture, and contamination. As Nagy [8] described, contamination may lead to the kissing bond - where adherend and adhesive bond are in intimate contact; however, there is no physical bonding at the interface. In other words, kissing bonds have complete physical contact with inadequate chemical bonding. While Brotherhood et al. [9] has categorized kissing bond as dry-contact and liquid layer, Jeenjitkaew and Guild [10] studied the drastic decrease in the integrity of adhesive and the bonding quality due to contamination, moisture and pure curing. After the work carried by Dillingham et al. [11] proposed the detection technique of the contaminations on the adherend surfaces prior to bonding with novel surface energy measurements via liquid drops, Crane et al. [12] studied to detect both airborne and contact type contaminations with this technique. Hereinafter called *weak bonds* precipitate unreliable behaviour and they are hardly detectable with NDT techniques as well as kissing bonds. In order to overcome the application limitations of adhesive

* Corresponding author.
E-mail address: bengisu.yilmaz@ktu.lt (B. Yılmaz).

https://doi.org/10.1016/j.ijadhadh.2020.102675
Received 24 April 2020; Accepted 12 June 2020
Available online 1 July 2020

joints and meet the safety requirements, it is essential to have reliable non-destructive testing methods.

There are numerous studies that discuss the evaluation of bonding quality with various non-destructive testing methods, yet only some of them focuses on the non-destructive detection and evaluation of weak bonds. Although longitudinal ultrasonic wave propagation is a conventional ultrasonic technique, the C-scan images have been used to demonstrate the manufacturing defects caused by moisture and humidity in adhesive joints by Markatos et al. [13]. It is stated that the change in quality reduction at the bonding interface can be detected if and only if the level of moisture is high enough. In addition, Titov et al. [14] uses pulse-echo ultrasonic non-destructive testing technique has been used to evaluate bonding quality with ultrasonic wave features and transmission-reflection coefficient calculations. Furthermore, Wang et al. [15] calculate the interfacial stiffness and transverse stiffness in order to evaluate weak bonds in PMMA-epoxy bonded structures has been studied with air-coupled ultrasound analytical models. However, the results are not always correlated with the experimental studies and the application to composites is very unlikely due to their nature of inhomogeneity and variety. Application of air-coupled ultrasound to evaluate bonding quality is limited due to high attenuation in air, high wavelength and low bandwidth nature; especially for composite bonded structures. Wu et al. [16] recently used air-coupled ultrasonic NDT systems to calculate interfacial stiffness of weak bonds in composite bonded structures during curing, however, the sensitivity of the study is only limited to curing related defects and the results need to be improved. Moreover, guided waves, especially lamb waves are used to evaluate the surface treatment effects not only on metal-adhesive bonded structures by Gauthier et al. [17] but also in composite-bonded structures by Ren and Lissenden [18]. The application of lamb wave investigations to composite materials is limited due to variations in dispersion curves of each structure. Moreover, the bond quality reduction had been correlated with nonlinearity level and had been investigated with nonlinear ultrasound by Yan et al. [19]. However, the application of the nonlinear ultrasonics is challenging in industrial applications. Additionally, Bossi et al. [20] has established that the laser bond inspection (LBI) could be used to eliminate weak and kissing bonds via transmitting concentrated shock waves into the adhesive layer. Furthermore, the detailed damage tolerance study of laser shock adhesion test (LASAT) technique for weak bond assessment was carried out by Ecault et al. [21] and Ehrhart et al. [22]. However, laser shock adhesion test (LASAT) and laser bond inspection (LBI) techniques are not yet universally available because the testing systems are expensive and costly to maintain. On the other hand, acoustic microscopy, with the high resolution as a result of high-frequency transducers and short wavelength, is found to be a promising ultrasonic NDT technique to investigate interface quality in bonded structures. Acoustic microscopy has been used as a non-destructive testing methodology for friction stir weld quality investigations with the combination of different NDT techniques such as X-ray tomography by Jasiuniene et al. [23] and holographic imaging by Twerdowski et al. [24].

The aim of this work is to evaluate the interface quality of composite-epoxy-composite single-lap joints with high-frequency acoustic microscopy. Novel post-processing algorithm has been proposed to highlight the weak bond determination in carbon fibre reinforced composite-epoxy single-lap joints. Three composite-adhesive joints having different bonding quality have been investigated along with the reference sample under laboratory conditions. The results show that the bonding quality variations, specifically interface quality variations, are clearly observed with high bonding characteristic values by the proposed techniques.

2. Sample description

Carbon fibre reinforced epoxy (CFRP)-epoxy-CFRP single-lap joints, containing four different bonding quality, have been produced at COTESA GmBH, Germany. Six layers of carbon-fibre reinforced epoxy from HexPly M21-5H Satin woven prepreg was manufactured as adherend. Resulting laminates have a thickness of 2.22 mm. Residual stress during lamination process caused variation in the thickness of composite plates in the range of 10^{-6} m. 3 M Scotch-Weld AF163 k-red structural adhesive film epoxy with the thickness of 0.24 mm has been selected as adhesive layer. The film adhesive has been placed on top of the CFRP adherends after surface preparation with acetone and grinding. Single-lap joints, containing four different bonding quality, including pristine state, had been produced. Adhesive bonding at pristine state has been manufactured without any inclusion as a reference sample and named “perfect bond” (Fig. 1 (A)). Secondly, five two-fold Wrigtlon 4600 release film inclusions having 12.7 mm edge length and 0.063 mm thickness has been placed on the interface of in between epoxy and top adherend to demonstrate “debonding” (Figs. 1, 2 (B)). Additionally, the adhesive film surface contaminated with the total amount of 0.6 mL of release agent Marbocote 45 using a spray as a representation of weak bond. Half of the sample has been masked during contamination in order to limit the amount of release agent contamination. The mask has been removed before the placement of the second adherend layer. The sample has been marked as “weak bond-less contamination” (Figs. 1, 2 (D)). On the other half of the sample, release agent uniformly diffused to the uncured epoxy layer and marked as “weak bond-more contamination” (Figs. 1, 2 (C)).

3. Scanning acoustic microscopy

Adhesively bonded CFRP-epoxy-CFRP single-lap joints containing four different bonding quality have been investigated with scanning acoustic microscopy (KSI GmBH) located in Ultrasound Research Institute, Kaunas University of Technology, Lithuania. The experimental set up shown in Fig. 3 has been used to save the ultrasonic response of the selected bonding areas of the samples. In the region of interest (16.7 mm $\times$ 16.7 mm square area on the bondline), 250 points on each Cartesian axis (x and y) has been measured and full time-scale A-scan response is recorded. Samples have been investigated with a 50 MHz focused ultrasonic transducer PT-50-3-10 under immersion with pulse-echo technique. Ultrasonic transducer aperture is 3 mm, and the focal distance in water is 10 mm (Fig. 3). During measurements, samples have been placed perpendicular to the transducer. The distance between the transducer and samples have been selected as 5.5 mm in order to focus the ultrasonic field on the interface of the sample.

Physical parameters such as the thickness and the ultrasonic wave velocity of the adherend play a significant role in order to select the correct transducer frequency that will be used for inspection. The higher the acoustic velocity in the adherend material, the shorter the time travel of acoustic wave; as well as thin adherend leads to shorter time travel of the acoustic wave. The conditions like high acoustic velocity and the small thickness of the adherend material create the need for ultrasonic inspections with higher frequency transducers.

It should be noted that high frequency investigations on highly attenuated materials such as composites depend on ultrasonic pulse ability to reach an interface of interest. The ratio between the thickness of the adherend, attention levels, and the focal distance of the transducer plays a significant role in the experimental performance.

4. Advanced post-processing algorithm

The high-frequency transducer selection combined with highly attenuating materials results in higher noise in the received signals. Therefore, the post-processing algorithms play a significant role in displaying meaningful ultrasonic responses of thin composite-adhesive bonded structures.

In this work, multi-level post-processing algorithm is used in order to evaluate bonding quality and detect weak bonds in composite-adhesive single-lap joints. The system diagram for the post-processing algorithm

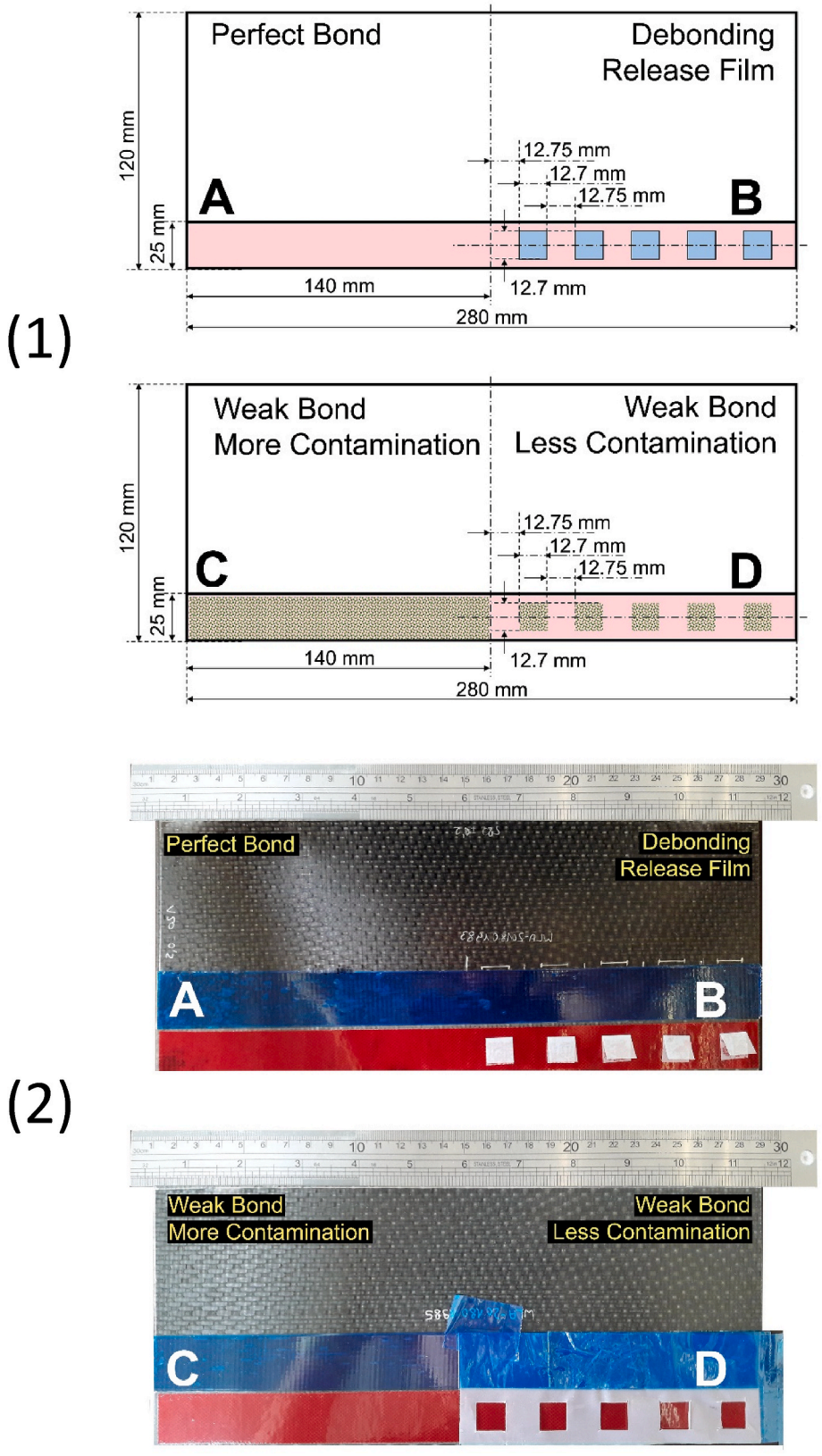

Fig. 1. CFRP-epoxy single-lap joints schematics (1) and pictures prior to bonding (2): (A) perfect bond, (B) debonding - release film inclusion, (C) weak bond with more release agent contamination, (D) weak bond - less release agent contamination.

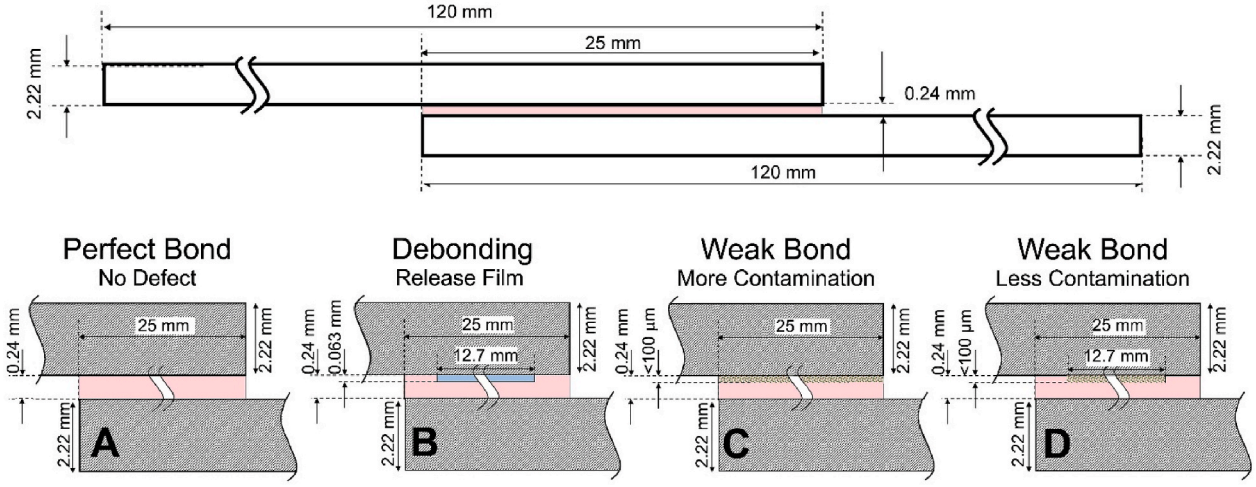

Fig. 2. CFRP-epoxy single-lap joints cross-section (not to scale) schematics: side view (top) and side view with zoom on the interface (bottom): (A) perfect bond, (B) debonding - release film inclusion, (C) weak bond with more release agent contamination, (D) weak bond with less release agent contamination.

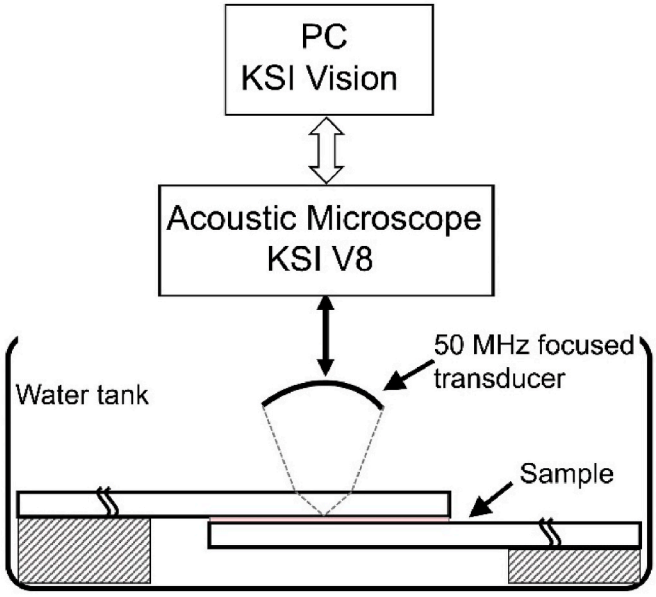

Fig. 3. Experimental set-up sketch for acoustic microscopy inspection of bonded specimens.

is shown in Fig. 4. As a start, A-scans have been recorded on the region of interest of bonded specimens. The electrical and structural noise has been removed from recorded A-scans with Wavelet denoising technique, suggested by Lazaro [25], where the level of denoising can be selected according to the input signal and central frequency of the transducer. Denoised signals have been aligned according to the surface reflection in order to eliminate the small variances due to the misplacement of the sample. Then, the time window of interest has been selected according to the calculated theoretical interface reflection of the bonded samples. In the time window of interests, the maximum values of A-scans have been aligned to be at the same time. Afterwards, amplitude and phase shift based visualization techniques have been applied to the data on time and frequency domains separately. As a result, four different two-dimensional images have been obtained to visualize the interface on the composite-adhesive bonded specimens.

4.1. Denoising

The recorded ultrasonic signal is noisy and scatters due to the anisotropic structure of the composite specimen, where the high-frequency transducer reckons more to the electronic noise. Therefore, there is a need for advanced denoising algorithm. Lazaro [25] studied the wavelet denoising which improves the detection rates in ultrasonic NDT and offers great flexibility. In this study, Symbol 3 – level 5 wavelets have been used with Stein's unbiased risk estimator (SURE) soft thresholding – which is data adaptive threshold estimator, where the residuals are kept at a minimum. Recorded A-scan signal with the denoised signal plotted on top is shown in Fig. 5.

4.2. Alignment and time window selection

In order to eliminate the small variations in the distance of sample surface position to the ultrasonic transducer, ultrasonic time of flight (ToF) of the surface reflection has been aligned according to −20 dB reflections. In the following equation, x is received ultrasonic surface reflection, i and j are the Cartesian coordinates of the transducer position

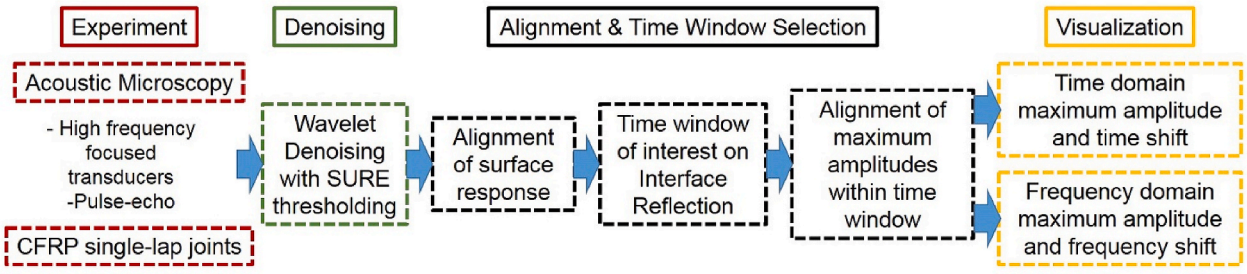

Fig. 4. System diagram for post-processing algorithm: Experiment, denoising, alignment and time window selection, visualization.

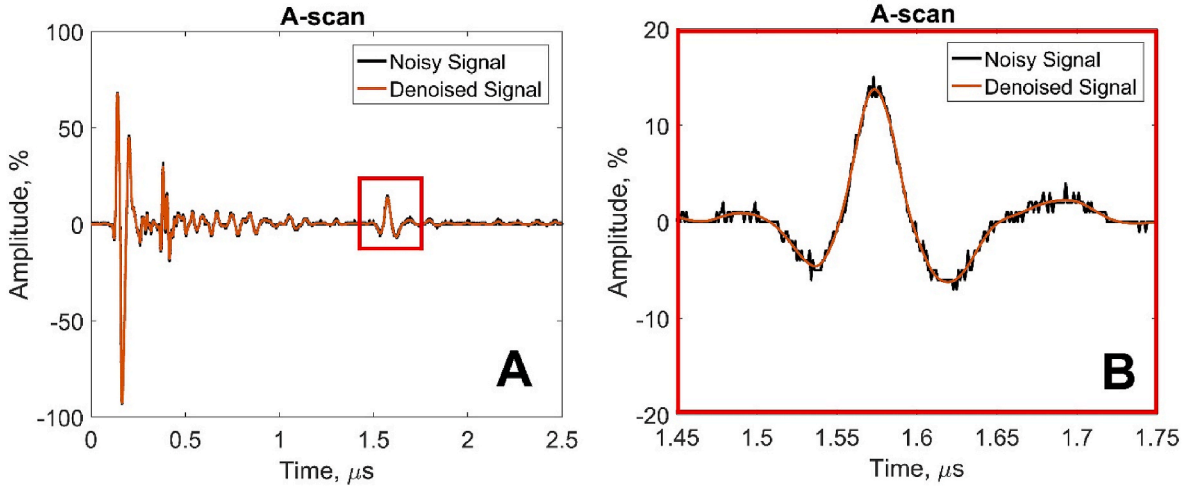

Fig. 5. Recorded A-scan example. Full time scale (A) and zoom on the interface reflection (B).

inside the region of interest, t is recorded time and t_0 is the time of flight where the zero crossing of each signal recorded (Equation (1)).

$$\tilde{x}^{ij}(t) = \begin{cases} x^{ij}(t)\,, & if\ x^{ij}(t_0) = -20\ dB \\ x^{ij}(t+a)\,, & if\ x^{ij}(t_0 - a) = -20\ dB \end{cases} \qquad \exists\, a : t \tag{1}$$

After eliminating surface abnormalities and the transducer position uncertainties from the data, theoretical time of flight (ToF) for interface reflection has been calculated in order to obtain interface quality information. As it is discussed in the previous section, transducer frequency plays an important role in order to be able to separate the interface reflection from internal reflections (Fig. 6). Also, derived from equation (2), the adherend thickness (T) and the ultrasonic wave velocity (c) inside the adherend determines the beginning of the time window of interest (t_{open}). In order to be consistent with the values of recorded signals, zero-crossing time has been added to the theoretically calculated time of flight.

$$t_{open} = t_0 + \frac{2T}{c} \tag{2}$$

The time window of interest begins with the calculated time of flight for the interface reflection (t_{open}). For closing the gate, the time duration of excitation pulse has been referenced and the time window length has been set to 150 ns in this case. Within the time window of interest, the data has been aligned for the second time according to the time corresponding to the maximum amplitude inside the time window of interest [3]. Following equations (equation (3), equation (4), equation (5)) demonstrate the alignment algorithm, where t_{max} is time value where the maximum ultrasonic response has been recorded within the time window of interest, x being the ultrasonic signal, t_{open} and t_{close} are the time window of interest opening and closing times respectively t_{center} is the mid-time inside the window of interest. As an example, recorded A-scan signals has been shown in Fig. 7 before and after the application of the alignment algorithm.

$$t_{center} = t_{open} + \left(\frac{t_{close} - t_{open}}{2}\right) \tag{3}$$

$$\max\left(\left|x^{ij}(t)\right|\right) = \mp\, x^{ij}(t_{max})\,, \quad t_{open} \le t \le t_{close} \tag{4}$$

$$\tilde{x}^{ij}(t) = \begin{cases} x^{ij}(t)\,, & if\ t_{center} = t_{max} \\ x^{ij}(t-a)\,, & if\ t_{center} = t_{max} + a \end{cases} \qquad \exists\, a : t \tag{5}$$

4.3. Interface visualization with data in time domain

After the alignments, two different interface quality representations in time domain has been obtained from data inside the time window of interest. Firstly, maximum amplitudes in the time window of interest have been calculated for each A-scan coordinate (C_{time}). Secondly, the deviation of the time of flight values where the maximum amplitude is observed within the time window with respect to t_{center}, which is the mid-time inside the window of interest, has been represented in order to check the performance of alignment algorithm at interface (P_{time}). Amplitude-time based interface visualization C_{time} is the C-scan image

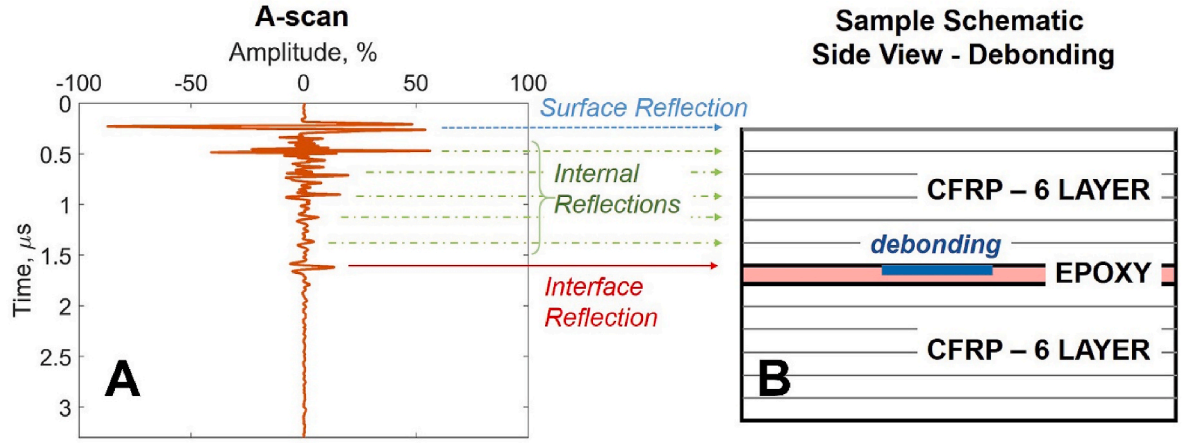

Fig. 6. Surface, internal, and interface reflections on the recorded A-scan signal (A) and the schematic of the sample (B).

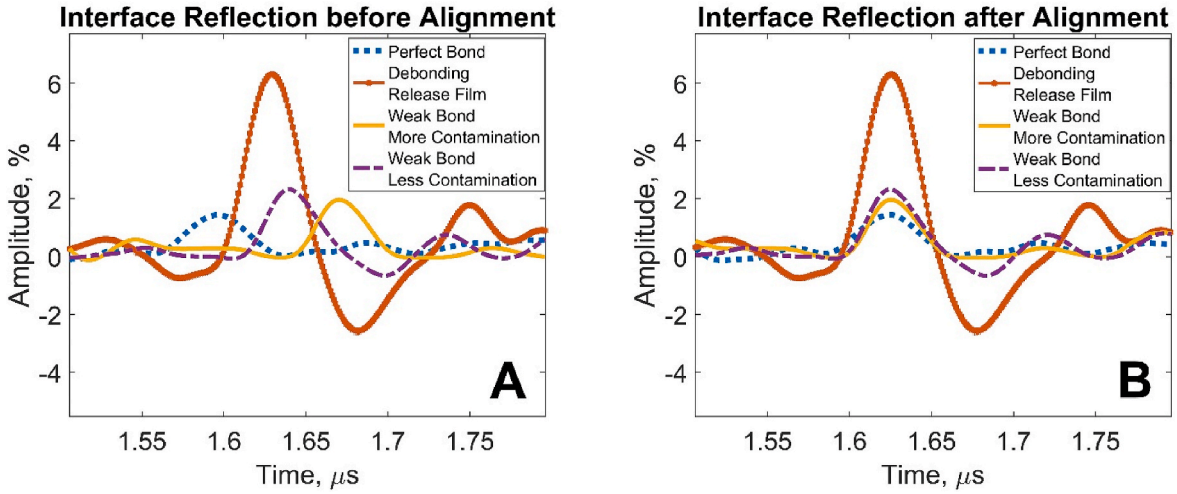

Fig. 7. A-scan signals on the time window of interest: (A) before alignment application (B) after alignment application.

values based on the maximum amplitudes in the time window of interest, phased-time based interface visualization P_{time} is the time shift based visualization to check the performance of the alignment, N is the number of recorded measurements i on lateral Cartesian coordinate, M is the number of recorded measurements j on longitudinal Cartesian coordinate.

$$C^{ij}_{time} = x^{ij}\,[t_{max}],\ \ \forall i\,\varepsilon\{1\ldots N\},\ \ \forall j\,\varepsilon\{1\ldots M\} \tag{6}$$

$$P^{ij}_{time} = |t_{max} - t_{center}|,\ \ \forall i\,\varepsilon\{1\ldots N\},\ \ \forall j\,\varepsilon\{1\ldots M\} \tag{7}$$

Equations (6) and (7) explains how the C-scan images from the data in the time domain have been obtained (amplitude-time based is in equation (6), phased-time based is in equation (7)). Fig. 8 shows how the pixel values for $\boldsymbol{C}_{time}$ and t_{max} values that is used to calculate $\boldsymbol{P}_{time}$ visualizations have been obtained from an example measurement point (i,j).

4.4. Interface visualization with data in frequency domain

After the alignments, two different interface quality representations in frequency domain has been obtained from the data within the time window of interest. Before visualization, data in the interface time window has been converted to the frequency spectrum. Next, amplitude-based representation from the maximum values that are observed in the frequency spectrum created amplitude-frequency based interface visualization $C_{frequency}$. Lastly, the frequency values that are corresponding to the maximum amplitude in the frequency domain have been represented as phase-frequency based interface visualization $P_{frequency}$.

$$\mathscr{F}\{x^{ij}[k]\} = Y^{ij}[k] = \sum_{m=0}^{n-1} x^{ij}[k]\omega_n^{jk},\ \ \forall i\,\varepsilon\{1\ldots N\},\ \ \forall j\,\varepsilon\{1\ldots M\} \tag{8}$$

In equation (8), Fourier transform has been shown by $\mathscr{F}\{x^{ij}\}$; where $\omega_n = e^{-2\pi\sqrt{-1}/n}$, $0 \le k < n$ and n is being the time duration inside the time window of interest $(t_{close} - t_{open})$ over sampling frequency.

$$|Y^{ij}[f^{ij}_{max}]| = \max(|Y^{ij}[f]|) \tag{9}$$

$$C^{ij}_{frequency} = Y^{ij}\,[f^{ij}_{max}],\ \forall i\,\varepsilon\{1\ldots N\},\ \forall j\,\varepsilon\{1\ldots N\} \tag{10}$$

$$P^{ij}_{frequency} = f^{ij}_{max},\ \ \forall i\,\varepsilon\{1\ldots N\},\ \ \forall j\,\varepsilon\{1\ldots N\} \tag{11}$$

Equations (10) and (11) demonstrates how the interface visualization from frequency domain based data has been obtained (amplitude-frequency based is in equation (10), phased-frequency based is in equation (11)). Fig. 9 shows how the pixel values for $\boldsymbol{C}_{frequency}$ and $\boldsymbol{P}_{frequency}$ visualizations has been obtained from an example measurement point (i,j).

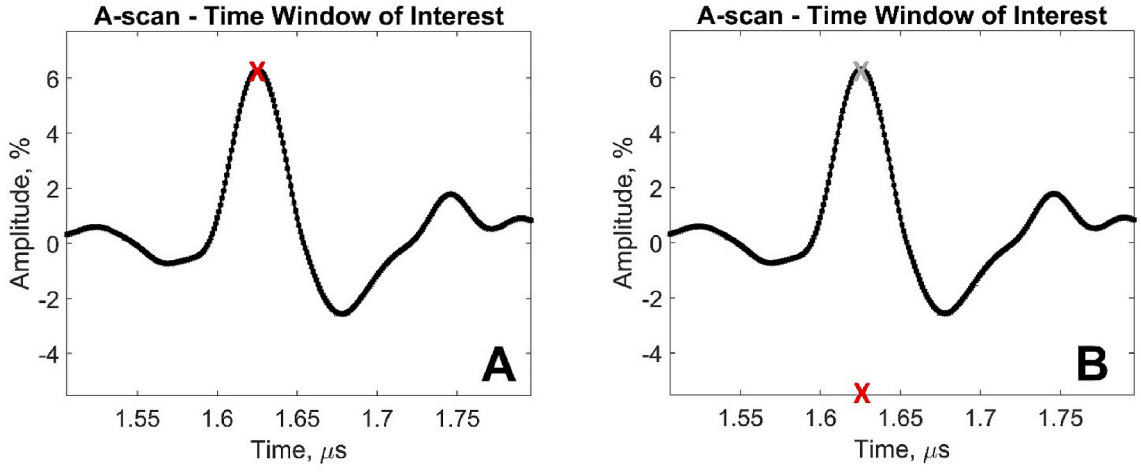

Fig. 8. A-scan signal on the time window of interest and the single point data that are used to visualize interface: for time-amplitude based interface visualization (A), for time-phased based visualization (B).

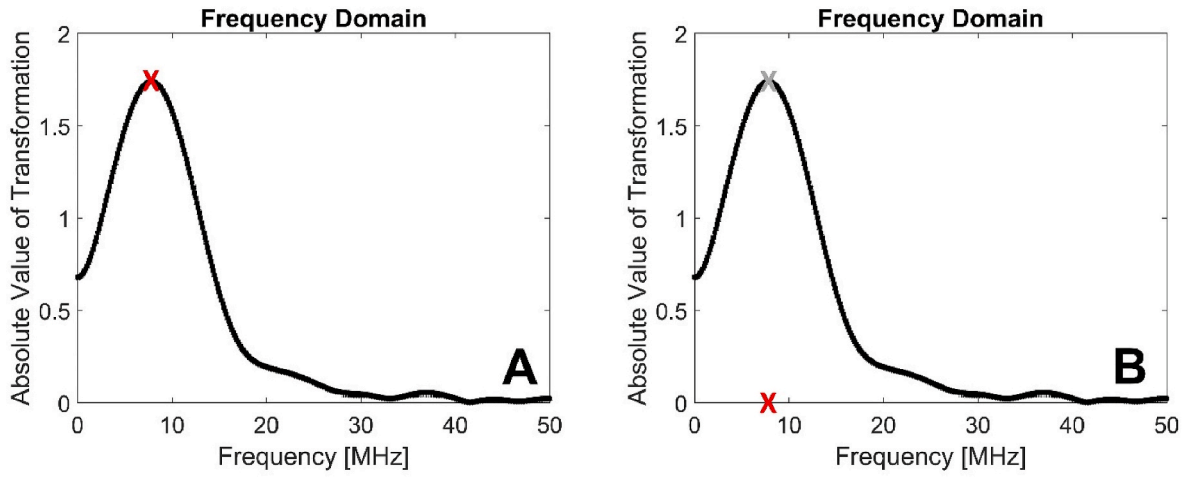

Fig. 9. F-scan signal on (signal in the time window of interest after Fourier transform) and the single point data that are used to visualize interface: for frequency-amplitude based interface visualization (A), for frequency-phased based visualization (B).

5. Non-destructive evaluation

Non-destructive evaluation of bonding quality has been performed on the scanning acoustic microscopy data by implementing the multi-level novel post-processing algorithm as the system diagram was shown in Fig. 4. After the application of multi-level post-processing algorithm, four different interface visualizations have been obtained ($\boldsymbol{C}_{time}$, $\boldsymbol{P}_{time}$, $\boldsymbol{C}_{frequency}$, $\boldsymbol{C}_{phase}$).

The first image obtained is time-amplitude based interface visualization $\boldsymbol{C}_{time}$ can be seen in Fig. 10 (A). This visualization depends on the maximum amplitude of ultrasonic response on each A-scan in the time domain within the time window of interest. As seen in Fig. 10 (A1), $\boldsymbol{C}_{time}$ visualization of perfect bond indicates no visible defect. On the other hand, Fig. 10 (A2) shows that debonding with release film can be detected by $\boldsymbol{C}_{time}$ visualization in composite-adhesive bonded structures with acoustic microscopy. Interface visualizations for the samples with weak bond with less contamination and weak bond with more contamination indicate some deviation compared to perfect bond visualization, however, it is very difficult to label them as defected or low bonding quality samples (Fig. 10 A3, A4).

Secondly, time-phased based interface visualization $\boldsymbol{P}_{time}$ shows the time of flight deviations of the observed maximum amplitudes in the time domain within the time window of interest (Fig. 10 (B)). This image visualizes the success or failure of the alignment procedure that has been applied in the time window of interest to interface reflection. As seen in Fig. 10 (B), having smaller values throughout the visualizations illustrates better reliability of the alignment algorithm since the algorithm requires that all maximum amplitudes (t_{max}) appear on the mid-time (t_{center}).

Third interface visualization $\boldsymbol{C}_{frequency}$ is amplitude-frequency based interface visualization where the observed maximum amplitude after the transition of the signal to frequency domain are represented (Fig. 10 (C)). The images for four different bonding quality, perfect bond, debonding with release film, weak bond less contamination and weak bond more contamination display quite similar results to the respective $\boldsymbol{C}_{time}$ interface visualizations. These similarities are expected since both $\boldsymbol{C}_{time}$ and $\boldsymbol{C}_{frequency}$ images are amplitude based visualizations, and the Fourier transform of the time domain data is amplitude dependent.

Last but not least, fourth interface image is obtained via phase-frequency based interface visualization $\boldsymbol{P}_{frequency}$ (Fig. 10 (D)). Pixel values on $\boldsymbol{P}_{frequency}$ images are the frequency values that is corresponding to the observed maximum amplitude in the frequency domain. In Fig. 10 (D1), perfect bond $\boldsymbol{P}_{frequency}$ image exhibits the sample is defect-free, while some variations are observed due to texture of the adhesive film layer. In Fig. 10 D2, debonding at the interface can be clearly identified as a defect. Weak bond less-contamination $\boldsymbol{P}_{frequency}$ interface visualization reveals defective zones on the interface (Fig. 10 D3). Compared to weak bond less contamination $\boldsymbol{P}_{frequency}$ image, weak bond more contamination $\boldsymbol{P}_{frequency}$ image shows less defective zones (Fig. 10 D4). This difference is expected due to the physical diffusion phenomenon of release agent contamination on the adhesive layer. It is expected that the mask used during the contamination procedure of weak bond less contamination sample has interrupted the diffusion procedure of release agent contaminant.

6. Quantitative performance evaluation of post-processing techniques

Both time and frequency based interface visualizations have been quantified according to the *bonding characteristic values* (BCV) which depend on the mean-square likelihood of observed values to the maximum observed value. Since maximum observed value corresponds to the high ultrasonic impedance difference at the interface, calculated bonding characteristic values results indicate the defect likelihood in each image. Results showing BCV ratios of four different bonding quality for four different post-processed visualizations have been reported in Table 1.

Bonding characteristic values for time-phase based interface visualization $\boldsymbol{P}_{time}$ evaluates the goodness of the alignment algorithm. Every pixel in $\boldsymbol{P}_{time}$ represents the deviation from mid-time where the algorithm supposed to align maximum ultrasonic amplitudes. Therefore, the smaller the values calculated by equation (12) indicates better performance in alignment algorithm.

For $\boldsymbol{C}_{time}$, $\boldsymbol{C}_{frequency}$, and $\boldsymbol{P}_{frequency}$ post-processing results, bonding characteristic values demonstrates the deviation from good joint in percentage over the inspected region of interest. For the defected samples namely debonding and weak bond, increase in bonding characteristic values express larger deviation from good joint. On the other hand $\boldsymbol{C}_{time}$, $\boldsymbol{C}_{frequency}$, and $\boldsymbol{P}_{frequency}$matrices represented for perfect bond with low bonding characteristic value illustrate high performance because the joint is good.

In Fig. 11, the bar graph represents the bonding characteristic values for different bonding quality composite-adhesive bonds for three different novel post-processing results. For frequency-amplitude based interface visualization $\boldsymbol{C}_{frequency}$, compared to traditional interface visualization technique $\boldsymbol{C}_{time}$, while the results for weak bond less contamination seems to be improved, they show slightly worse performance for other bonding quality samples. On the other hand, a significant increase in the performance has been observed for the phase-frequency based

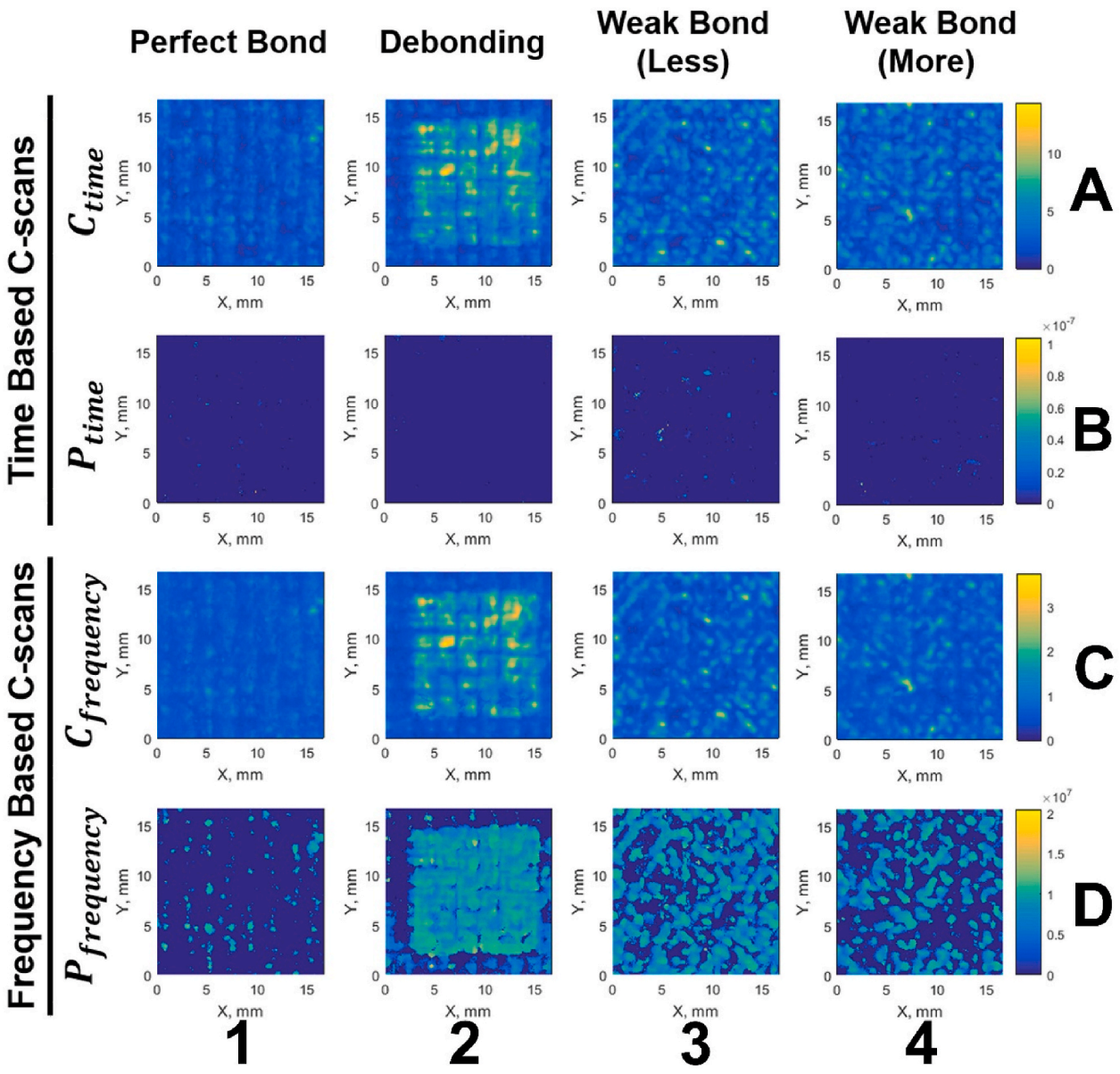

Fig. 10. Interface visualizations after multi-level post-processing algorithm (amplitude-time based (A), phase-time based (B), amplitude-frequency based (C), phase-frequency based (D)) for four different bonding quality (perfect bond (1), debonding with release film contamination (2), weak bond with less release agent contamination (3), weak bond with more release agent contamination (4)).

Table 1
Bonding characteristic values in percentile for the post-processed results.

Interface visualization		Bonding Quality:			
		Perfect Bond	Debonding (release film)	Weak bond (more contamination)	Weak bond (less contamination)
Time domain	C_{time}	3.68%	20.69%	8.23%	9.26%
	P_{time}	0.030%	0.008%	0.026%	0.134%
Frequency domain	$C_{frequency}$	4.27%	19.93%	7.14%	8.21%
	$P_{frequency}$	1.59%	23.89%	10.83%	19.52%

interface visualization $\boldsymbol{P}_{frequency}$ (Fig. 11). Specifically, weak bond less-contamination results with $\boldsymbol{P}_{frequency}$ shows high defect detection bonding characteristic values compared to weak-bond more contamination results with the same visualization technique.

$$BCV = \frac{\sum_{i=1}^{N}\sum_{j=1}^{M}\left(C^{ij}\right)^2}{\sum_{i=1}^{N}\sum_{j=1}^{M}\left(\max\left(C^{ij}\right) - C^{ij}\right)^2} x100 \quad (12)$$

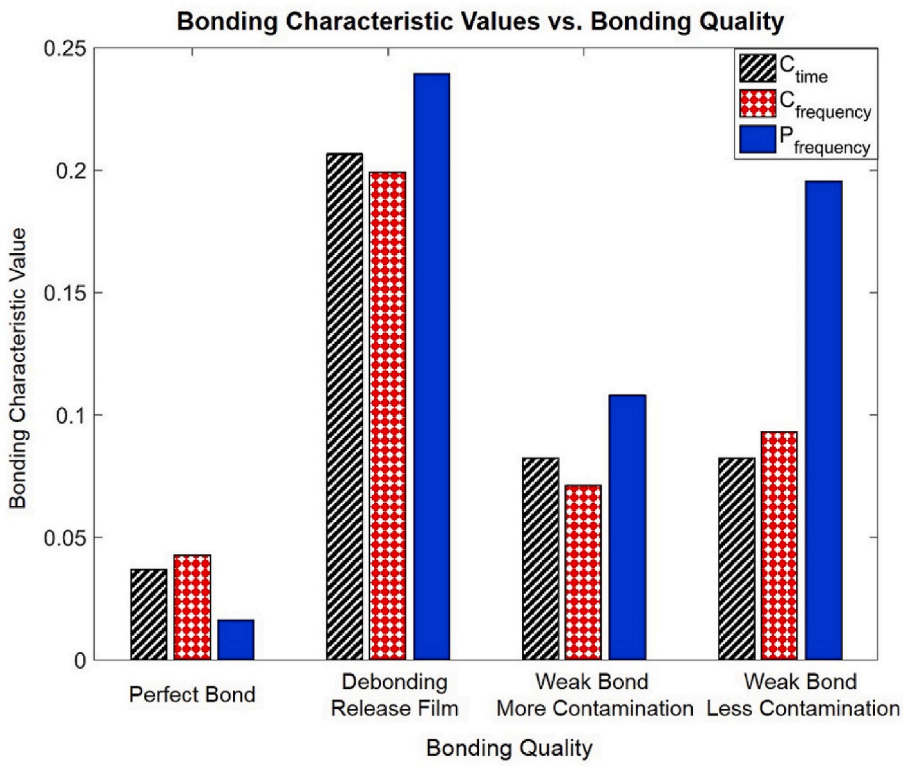

Fig. 11. Bonding characteristic values for defect detection along with different bonding quality samples and different post-processing results: time-amplitude based interface visualization performance (black-diagonal striped), frequency-amplitude based interface visualization performance (red-checked pattern), and frequency-phase based interface visualization performance (blue-plain pattern). (For interpretation of the references to colour in this figure legend, the reader is referred to the Web version of this article.)

7. Conclusions

The non-destructive evaluation of the quality of the composite-epoxy adhesive bond is challenging because the adhesion phenomenon occurs in a thin interface where the contamination that decreases the quality is also located. However, these contaminations must be detected because even small amounts may deteriorate the joint performance significantly. Characterization of small amounts of contamination is still challenging for conventional ultrasonic techniques due to similar acoustical impedance of contaminated interface and adhesives. It was determined that, developed novel post-processing algorithm with high frequency focused transducers used in acoustic microscopy is capable to visualize interface quality in composite-epoxy adhesive bonded structures. In addition, independent of the perfect bond inspection results, novel post-processing algorithm performs well to detect weak bond.

In this work, carbon-fibre reinforced epoxy-epoxy single-lap adhesive joints with three different bonding quality and pristine state have been investigated using acoustic microscopy. Advanced quantitative post-processing algorithm has been developed and applied to the experimental results. Investigations show that high frequency ultrasonic transducers can capture the interface quality in composite-epoxy adhesive joints and the developed post-processing algorithm enables the detection of weak bonds.

Using the developed post-processing algorithm, four different interface visualization images have been obtained for samples with different bonding quality. Comparing four different algorithms, time-phase based interface visualization P_{time} shows the goodness of the algorithm, therefore it is excluded from defect detection performance calculations. Time-amplitude based interface visualization C_{time} can be considered as conventional interface visualization, which mostly shows the maximum of the observed amplitude values in the time window of interest. Frequency-time based interface visualization $C_{frequency}$ is expected to show similar results to the conventional algorithm due to the amplitude dependence of the Fourier transform. However, frequency-phase based interface visualization $P_{frequency}$ demonstrates a novel technique to evaluate bonding quality. The qualitative results have also been compared with the quantitative bonding characteristic value calculations.

Analysing the frequency-phase based interface visualizations obtained using the developed algorithm, it is also observed that, the less contaminated regions show more defective zones than the more contaminated regions. It is expected that the diffusion of release agent into the adhesive film has been more dominant at more contaminated regions of the sample, on the other hand, the less contaminated regions had more release agent on the interface.

It was shown that the novel post-processing algorithm extracts more information on the evaluation of bonding quality. The presented results prove that the high-frequency acoustic microscopy with developed post-processing algorithm is a great candidate to evaluate bonding quality and detect weak bonds that occur due to bonding interface contamination. However, the limitations regarding structure dimensions and water immersion should be noted.

This study opens the discussion of possible post-processing algorithms that might help to detect weak bonds that occur due to contamination, yet, different bonding qualities such as kissing bond should be studied separately. The proposed novel post-processing algorithm could be utilized for the evaluation of the bonding quality in adhesive joints not only in aerospace structures but also in different industries such as automotive and marine, as adhesive joints are gaining their popularity and are used more and more.

Funding

This work was supported by NDTonAIR project from the European Union's Horizon 2020 research and innovation program under the Marie Sklodowska-Curie [grant number 722134].

References

[1] Scarselli G, Corcione C, Nicassio F, Maffezzoli A. Adhesive joints with improved mechanical properties for aerospace applications. Int J Adhesion Adhes 2017. https://doi.org/10.1016/j.ijadhadh.2017.03.012.

[2] Budhe S, Banea MD, de Barros S, da Silva LFM. An updated review of adhesively bonded joints in composite materials. Int J Adhesion Adhes 2017;72:30–42. https://doi.org/10.1016/j.ijadhadh.2016.10.010.

[3] Jasiūnienė E, Mažeika L, Samaitis V, Cicėnas V, Mattsson D. Ultrasonic non-destructive testing of complex titanium/carbon fibre composite joints. Ultrasonics 2019. https://doi.org/10.1016/j.ultras.2019.02.009.

[4] Tornow C, Schlag M, Lima LCM b, Stübing D, Hoffmann M, Noeske P-LM, et al. Quality assurance concepts for adhesive bonding of composite aircraft structures-characterisation of adherent surfaces by extended NDT. J Adhes Sci Technol 2015; 29:2281–94. https://doi.org/10.1080/01694243.2015.1055062.

[5] Adams RD, Drinkwater BW. Nondestructive testing of adhesively-bonded joints. NDT E Int 1997;30:93–8. https://doi.org/10.1016/S0963-8695(96)00050-3.

[6] Vine K, Cawley P, Kinloch AJ. The correlation of non-destructive measurements and toughness changes in adhesive joints during environmental attack. J Adhes 2001;77:125–61. https://doi.org/10.1080/00218460108030735.

[7] Adams RD, Cawley P. A review of defect types and nondestructive testing techniques for composites and bonded joints. NDT E Int 1991;24:105. https://doi.org/10.1016/0963-8695(91)90924-R.

[8] Nagy PB. Ultrasonic detection of kissing bonds at adhesive interfaces. J Adhes Sci Technol 1991;5:619–30. https://doi.org/10.1163/156856191X00521.

[9] Brotherhood CJ, Drinkwater BW, Guild FJ. The effect of compressive loading on the ultrasonic detectability of kissing bonds in adhesive joints. J Nondestr Eval 2002;21:95–104. https://doi.org/10.1023/A:1022584822730.

[10] Jeenjitkaew C, Guild FJ. The analysis of kissing bonds in adhesive joints. Int J Adhesion Adhes 2017;75:101–7. https://doi.org/10.1016/j.ijadhadh.2017.02.019.

[11] Dillingham G, Oakley B, Voast PJV, Shelley PH, Blakley RL, Smith CB. Quantitative detection of peel ply derived contaminants via wettability measurements. J Adhes Sci Technol 2012;26:1563–71. https://doi.org/10.1163/156856111X618416.

[12] Crane R, Dillingham G, Oakley B. Progress in the reliability of bonded composite structures. Appl Compos Mater 2017;24:221–33. https://doi.org/10.1007/s10443-016-9523-2.

[13] Markatos DN, Tserpes KI, Rau E, Markus S, Ehrhart B, Pantelakis S. The effects of manufacturing-induced and in-service related bonding quality reduction on the mode-I fracture toughness of composite bonded joints for aeronautical use. Compos B Eng 2013;45:556–64. https://doi.org/10.1016/j.compositesb.2012.05.052.

[14] Titov SA, Maev RG, Bogachenkov AN. Pulse-echo NDT of adhesively bonded joints in automotive assemblies. Ultrasonics 2008;48:537–46. https://doi.org/10.1016/j.ultras.2008.07.001.

[15] Wang XG, Wu WL, Huang ZC, Chang JJ, Wu NX. Research on the transmission characteristics of air-coupled ultrasound in double-layered bonded structures. Materials 2018;11. https://doi.org/10.3390/ma11020310.

[16] Wu W-L, Wang X-G, Huang Z-C, Wu N-X. Measurements of the weak bonding interfacial stiffness by using air-coupled ultrasound. AIP Adv 2017;7:125316. https://doi.org/10.1063/1.5001248.

[17] Gauthier C, Ech-Cherif El-Kettani M, Galy J, Predoi M, Leduc D. Structural adhesive bonding characterization using guided Lamb waves and the vertical modes. Int J Adhesion Adhes 2020. https://doi.org/10.1016/j.ijadhadh.2019.102467.

[18] Ren B, Lissenden CJ. Ultrasonic guided wave inspection of adhesive bonds between composite laminates. Int J Adhesion Adhes 2013;45:59–68. https://doi.org/10.1016/j.ijadhadh.2013.04.001.

[19] Yan D, Drinkwater BW, Neild SA. Measurement of the ultrasonic nonlinearity of kissing bonds in adhesive joints. NDT E Int 2009;42:459–66. https://doi.org/10.1016/j.ndteint.2009.02.002.

[20] Bossi R, Lahrman D, Sokol D, Walters C. Laser Bond Inspection for adhesive bond strength. Int. SAMPE Tech. Conf. 2011:11. SAMPE 2011, May.

[21] Ecault R, Boustie M, Touchard F, Pons F, Berthe L, Chocinski-Arnault L, et al. A study of composite material damage induced by laser shock waves. Compos Part A Appl Sci Manuf 2013. https://doi.org/10.1016/j.compositesa.2013.05.015.

[22] Ehrhart B, Ecault R, Touchard F, Boustie M, Berthe L, Bockenheimer C, et al. Development of a laser shock adhesion test for the assessment of weak adhesive bonded CFRP structures. Int J Adhesion Adhes 2014;52:57–65. https://doi.org/10.1016/j.ijadhadh.2014.04.002.

[23] Jasiūnienė E, Žukauskas E, Dragatogiannis DA, Koumoulos EP, Charitidis CA. Investigation of dissimilar metal joints with nanoparticle fillers. NDT E Int 2017. https://doi.org/10.1016/j.ndteint.2017.08.005.

[24] Twerdowski E, von Buttlar M, Grill W. Scanning acoustic defocused transmission microscopy with vector contrast combined with holography for weak bond imaging. Heal Monit Smart Nondestruct Eval Struct Biol Syst V 2006;6177:617718. https://doi.org/10.1117/12.657881.

[25] Lazaro JC. Noise reduction in ultrasonic NDT using discrete wavelet transform processing. 2002 IEEE Ultrason. Symp. 2002. Proceedings. 2002;1:777–80. https://doi.org/10.1109/ULTSYM.2002.1193514. IEEE.